Green-Mediated Synthesis of NiCo2O4 Nanostructures Using Radish White Peel Extract for the Sensitive and Selective Enzyme-Free Detection of Uric Acid

Abdul Ghaffar Solangi, Aneela Tahira, Baradi Waryani, Abdul Sattar Chang, Tajnees Pirzada, Ayman Nafady, Elmuez A Dawi, Lama Saleem, Mohsen Padervand, Abd Al Karim Haj Ismail, et al.

biosensors

MDPI

Article

Green-Mediated Synthesis of $NiCo_2O_4$ Nanostructures Using Radish White Peel Extract for the Sensitive and Selective Enzyme-Free Detection of Uric Acid

Abdul Ghafar Solangi [1], Aneela Tahira [1], Baradi Waryani [9], Abdul Sattar Chang [2], Tajnees Pirzada [1], Ayman Nafady [5], Elmuez A. Dawi [8], Lama M. A. Saleem [7], M. Padervand [7], A. Haj Ismail [8], Kangle LV [9], Brigitte Vigolo [6] and Zafar Hussain Ibupoto [2,*]

[1] Institute of Chemistry, Shah Abdul Latif University Khairpur Mirs, Khairpur Mirs 66111, Sindh, Pakistan; ghaffarchemistry786@gmail.com (A.G.S.); aneela.tahira@salu.edu.pk (A.T.); tajnees@salu.edu.pk (T.P.)
[2] Institute of Chemistry, University of Sindh, Jamshoro 76080, Pakistan; asattar.chang@usindh.edu.pk (A.S.C.)
[3] Department of Fresh Water Biology and Fisheries, University of Sindh, Jamshoro, Sindh, Pakistan; baradiw@usindh.edu.pk
[4] Department of Chemistry, Faculty of Science, University of Maragheh, Maragheh P.O. Box. 55181-83111, Iran; padervand@maragheh.ac.ir
[5] Department of Chemistry, College of Science, King Saud University, Riyadh 11451, Saudi Arabia; anafady@ksu.edu.sa
[6] *Institut Jean Lamour,* Université de Lorraine, CNRS, IJL, F-54000 Nancy, France; brigitte.vigolo@univ-lorraine.fr
[7] Biomolecular Science, Earth and Life Science, Amsterdam University, De Boelelaan 1105/1081, HV Amsterdam, The Netherlands; lamysaleem@gmail.com
[8] Nonlinear Dynamics Research Centre (NDRC), Ajman University, Ajman P.O. Box 346, United Arab Emirates; e.dawi@ajman.ac.ae (E.A.D.); a.hajismail@ajman.ac.ae (A.H.I.)
[9] College of Resource and Environment, South-Central Minzu University, Wuhan 430074, China; lvkangle@mail.scuec.edu.cn
* Correspondence: zaffar.ibhupoto@usindh.edu.pk

Citation: Solangi, A.G.; Tahira, A.; Waryani, B.; Chang, A.S.; Pirzada, T.; Nafady, A.; Dawi, E.A.; Saleem, L.M.A.; Padervand, M.; Haj Ismail, A.; et al. Green-Mediated Synthesis of $NiCo_2O_4$ Nanostructures Using Radish White Peel Extract for the Sensitive and Selective Enzyme-Free Detection of Uric Acid. *Biosensors* **2023**, *13*, x. https://doi.org/10.3390/xxxxx

Received: 27 June 2023
Revised: 25 July 2023
Accepted: 30 July 2023
Published: date

Abstract: The ability to measure uric acid (UA) non-enzymatically in human blood has been demonstrated through the use of a simple and efficient electrochemical method. A phytochemical extract from radish white peel extract improved the electrocatalytic performance of nickel–cobalt bimetallic oxide ($NiCo_2O_4$) during a hydrothermal process through abundant surface holes of oxides, an alteration of morphology, an excellent crystal quality, and increased Co(III) and Ni(II) chemical states. The surface structure, morphology, crystalline quality, and chemical composition were determined using a variety of analytical techniques, including powder X-ray diffraction (XRD), scanning electron microscopy (SEM), high-resolution transmission electron microscopy (HR-TEM), and X-ray photoelectron spectroscopy (XPS). The electrochemical characterization by CV revealed a linear range of UA from 0.1 mM to 8 mM, with a detection limit of 0.005 mM and a limit of quantification (LOQ) of 0.008 mM. A study of the sensitivity of $NiCo_2O_4$ nanostructures modified on the surface to UA detection with amperometry has revealed a linear range from 0.1 mM to 4 mM for detection. High stability, repeatability, and selectivity were associated with the enhanced electrochemical performance of non-enzymatic UA sensing. A significant contribution to the full outperforming sensing characterization can be attributed to the tailoring of surface properties of $NiCo_2O_4$ nanostructures. EIS analysis revealed a low charge-transfer resistance of 114,970 Ohms that offered $NiCo_2O_4$ nanostructures prepared with 5 mL of radish white peel extract, confirming an enhanced performance of the presented non-enzymatic UA sensor. As well as testing

the practicality of the UA sensor, blood samples from human beings were also tested for UA. Due to its high sensitivity, stability, selectivity, repeatability, and simplicity, the developed non-enzymatic UA sensor is ideal for monitoring UA for a wide range of concentrations in biological matrixes.

Keywords: non-enzymatic uric acid sensor; phytochemicals; radish white peel extract; biological matrix

1. Introduction

A purine-based compound called alkaloids is used by our bodies to produce uric acid (UA) [1,2]. UA concentrations in serum samples range between 0.13 and 0.46 mM, whereas UA concentrations in urine samples range between 1.49 and 4.50 mM [3]. An abnormal level of UA in the human body is associated with several chronic and life-threatening diseases, including preeclampsia, arthritis, renal dysfunction, cardiovascular disease, obesity, high blood pressure, and kidney disease [4–7]. An increase in UA levels in blood serum has been identified as a major cause of cardiac disease [8]. For this reason, it is essential to measure and monitor UA in order to prevent the onset of dangerous conditions and to reduce the risk of premature death. Several analytical methods have been developed to measure UA as a result of this high importance, including colorimetric enzymatic tests [9]. Capillary electrophoresis method [10], surface-enhanced Raman scattering [11], liquid chromatography [12], electrochemical method [13], fluorescence spectroscopy [14], and chemiluminescence [15] are among the methods used. It is common for these analytical methods to be extremely expensive, time-consuming, and complex to operate. However, electrochemical methods are inexpensive, sensitive, and selective, thus they have been extensively studied [16–21]. A number of electrochemical approaches have been used to quantify UA's high electrooxidation properties, including enzyme-based and enzyme-free methods [22–26]. Due to the high costs associated with enzyme immobilization and denatured issues with uricase enzyme during storage, non-enzymatic approaches have become increasingly popular as alternatives to enzyme-based approaches [27]. In non-enzymatic approaches, highly electrocatalytic materials are always desirable [18,16]. To realize non-enzymatic UA sensors quickly, it will be increasingly necessary to develop new materials with tailored surfaces that outperform electrocatalytic properties. This task, however, appears to be challenging because novel materials with tailored surfaces do not possess electrocatalytic properties. For the development of highly catalytic materials for non-enzymatic UA sensors, several challenges must be overcome, such as poor electrical conductivity, a limited number of catalytic sites, and chemical stability concerns. Therefore, numerous electrocatalytic materials have been developed and investigated for the development of non-enzymatic sensors [28–31]. A significant electrochemical activity of metal oxides makes them potentially suitable for this application [32–34]. As a result of its high electrical conductivity and favorable redox properties, a bimetallic oxide, particularly nickel–cobalt oxide ($NiCo_2O_4$), has been identified as a potential candidate for the development of non-enzymatic sensors. As $NiCo_2O_4$ nanostructures exhibit poor electrochemical performance due to their limited surface properties, they have been utilized in composites with other nanostructured materials, such as Fe_2O_3 @ $NiCo_2O_4$ [35], $MnO_2/NiCo_2O_4$ [36], $Co_3O_4/NiCo_2O_4$ [37,38], and $NiCo_2O_4$ @ graphene [39]. It has been observed that composite $NiCo_2O_4$ systems exhibit enhanced charge transfer between electrode and analyte. Several morphologies of $NiCo_2O_4$ have been prepared, including nanotubes [37], nanorods [36], nanospheres [35], and nanosheets [33]. In spite of $NiCo_2O_4$'s diverse architecture, however, the material fails to perform as expected [35,36,38]. As a result, it is imperative to identify new strategies for improving the elec-

trochemical performance of $NiCo_2O_4$ in order to develop more sensitive non-enzymatic UA sensors. Recent years have seen a great deal of interest in green chemistry due to its simplicity, eco-friendliness, low cost, and environmental friendliness [39–42]. Several natural products obtained from biomass wastes can be used to tailor the surface properties of nanostructured materials, including catalytic sites and charge transfer properties [41,42]. Only a few studies have been conducted on the synthesis of $NiCo_2O_4$ nanostructured materials from biomass wastes. The present study examines for the first time the effect of radish white peel extract (*Raphanus sativus*) on the morphology, crystal defect, and surface properties of $NiCo_2O_4$ that will be used for fabricating a non-enzymatic UA sensor. Radish white peel extract contains a wide range of phytochemicals, including alkaloids, glucosinolates, phenolic compounds, organic acids, anthocyanins, and isothiocyanates. [40,41] (Scheme 1).

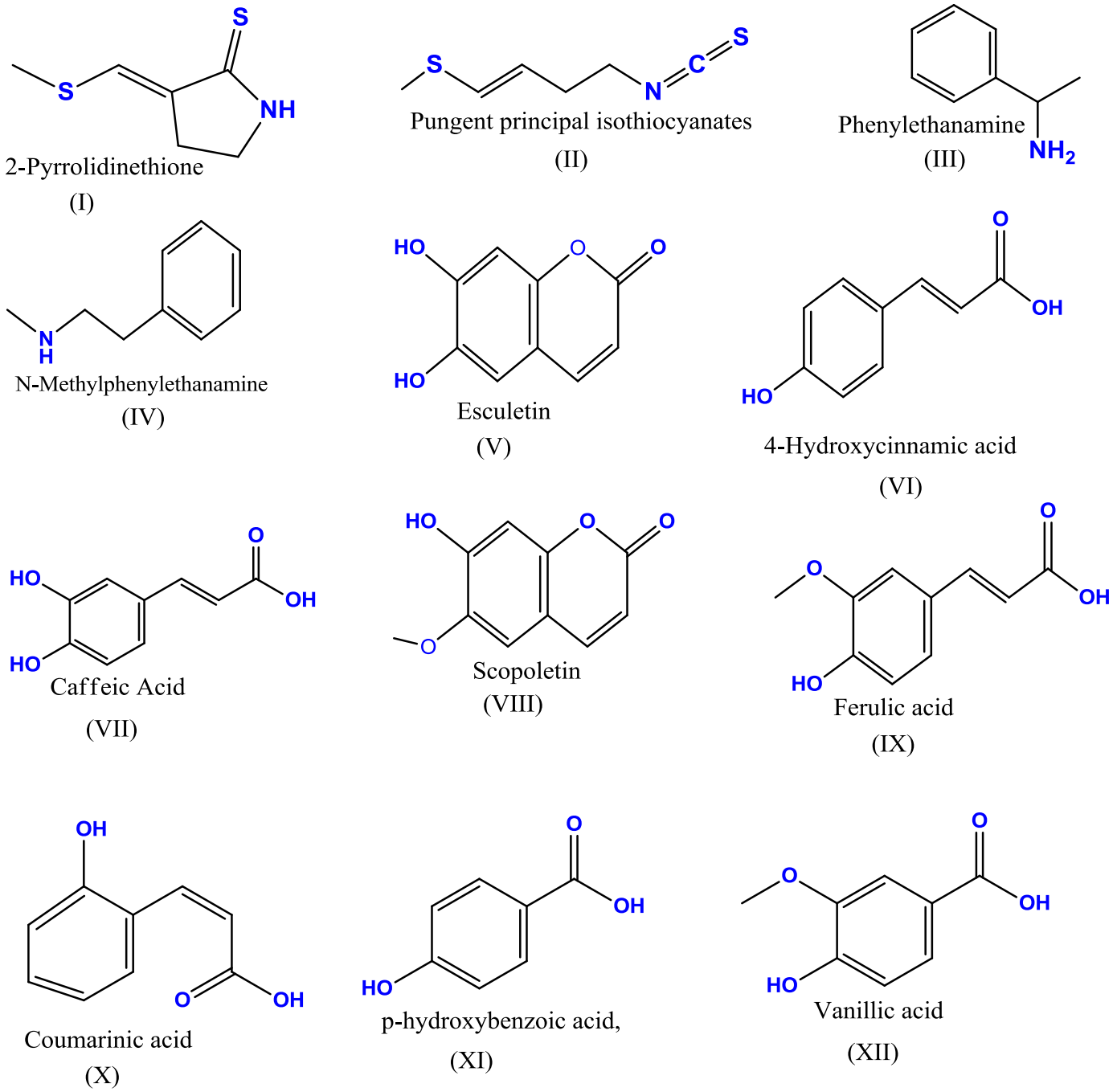

Scheme 1. The various phytochemicals present in the radish ((*Raphanus sativus*) peel extract.

The radish white peel extract possesses major phytochemicals, like as 4-hydroxycinnamic acid, caffeic acid, ferulic acid, and isothiocyanates, which were used as stabilizing, capping, and reducing agents, and played a significant role toward enhanced electrochemical properties of $NiCo_2O_4$ nanostructures.

In this study, we have used radish white peel extracts for the surface engineering of $NiCo_2O_4$ nanostructures by hydrothermal methods. The volume of extracts from peels was examined in order to determine the ideal concentration at which $NiCo_2O_4$ nanostructures could be scaled up for high performance production. An extensive linear range of UA detection was detected using surface-modified $NiCo_2O_4$ nanostructures ranging from 0.1 mM to 8 mM.

2. Experimental Section

2.1. Chemicals Used

In this study, cobalt chloride hexahydrate ($CoCl_2.6H_2O$), nickel chloride hexahydrate ($NiCl_2.6H_2O$), glucose, lactic acid, uric acid, sodium chloride, potassium chloride, ascorbic acid, sodium hydroxide, urea, hydrochloric acid, disodium phosphate, and monopotassium phosphate were applied without pretreatment. We obtained all analytical grade chemical reagents from Sigma Aldrich, Karachi, and Sindh Pakistan. UA detection was performed by preparing the desired solutions in deionized water, followed by preparing a buffer solution containing 0.1 M phosphate at pH 7.0 for UA detection.

2.2. Green-Mediated Synthesis of $NiCo_2O_4$ Nanostructures Using Radish White Peel Extract

A hydrothermal method was used for phytochemical synthesis of $NiCo_2O_4$ nanostructures. The radish white was purchased, washed with deionized water, and allowed to dry at room temperature prior to the growth process. Small pieces of radish white were chipped after the peel had been removed. An automatic juicer was then used to collect juice from the peel. An extract of the peel was used in the subsequent synthesis of $NiCo_2O_4$ nanostructures. $NiCo_2O_4$ nanostructures were prepared using 0.1 M cobalt chloride hexahydrate, 0.1 M urea, and 0.015 M nickel chloride hexahydrate in 100 mL of deionized water through a hydrothermal process. Various amounts of radish white peel extract were used to synthesize $NiCo_2O_4$ nanostructures. The pH of the precursor solution was 8.2 and 7.1, respectively. Afterward, the growth solutions were sealed with aluminum sheets and grown at 95 °C for five hours. Filter paper was used to collect the bimetallic hydroxide phase, and deionized water was used to wash it several times. The material was then thermally roasted for five hours at 500 °C after drying for 12 h. With the same procedure, pristine $NiCo_2O_4$ nanostructures were obtained without adding radish white peel extract. An illustration of the synthesis of $NiCo_2O_4$ nanostructures as prepared can be found in Scheme 2.

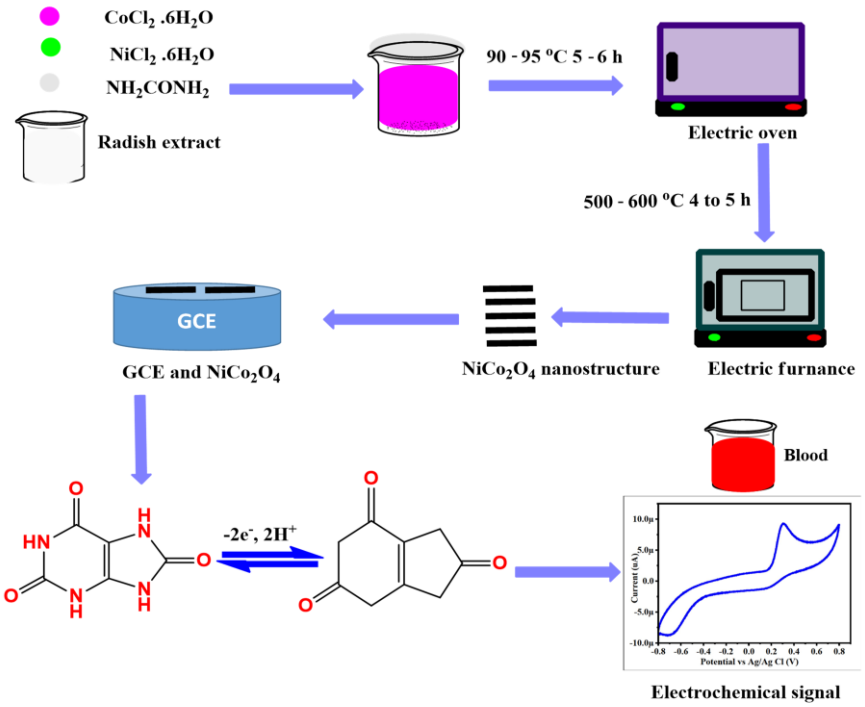

Scheme 2. Stepwise synthesis of $NiCo_2O_4$ nanostructures using radish white peel extract during hydrothermal method, UA detection, and real blood sample analysis.

2.3. Physical Investigations on the Surface-Modified $NiCo_2O_4$ Nanostructures

An assessment of the morphology of $NiCo_2O_4$ nanostructures was carried out by scanning electron microscopy (SEM: JEOL Japan Model No. JSM-IT 100, Auto Fine Coater: JEC-3000FC; the coating performed at 20 mA current for 60 s) using an accelerating voltage of 10 kV. We assessed the crystal quality of radish white peel extract-assisted $NiCo_2O_4$ nanostructures using powder X-ray diffraction (XRD) at 45 kV and 45 mA using CuK radiation (λ = 1.5418 Å) as an X-ray source. The localized nanoscale structure was studied using high-resolution transmission electron microscopy (HRTEM) at a voltage of 200 kV. Utilizing energy dispersive spectroscopy, we were able to quantify the elemental mapping. The chemical composition of the surface was determined using X-ray photoelectron spectroscopy (XPS) in high vacuum. As a reference binding energy, we calibrated the XPS data using C1s at 284.6 eV and deconvolved the XPS features using a Shirley-type background and Voigt curves.

2.4. Non-Enzymatic Sensing of UA onto Surface-Modified $NiCo_2O_4$ Nanostructures

A variety of electrochemical methods have been used to characterize the non-enzymatic UA sensor, including cyclic voltammetry, amperometry, electrochemical impedance spectroscopy, and linear sweeping voltammetry. The electrochemical evaluation of $NiCo_2O_4$ nanostructures was conducted using a three-electrode setup. Three electrodes were used: silver–silver chloride (Ag/AgCl, 3.0 M KCl) as a reference electrode, platinum sheet as a counter electrode, and glassy carbon electrode (GCE) as a working electrode. Prior to modification of the GCE, it was polished with an alumina paste of (0.3 μM) and silicon paper and then cleaned with deionized water. The material ink was prepared by dispersing 10 mg of $NiCo_2O_4$ nanostructures in 2.5 m of deionized water and 0.5 mL of Nafion (5%) in 2.5 m of deionized water. We achieved homogeneous material ink after 15 min of an ultrasonic bath. $NiCo_2O_4$ nanostructures were applied to the surface of GCE using a drop-cast method. A 10 mM stock solution of UA was pre-

pared in a 0.1 M phosphate buffer solution of pH 7.0. Prior to dissolving the phosphate buffer solution, UA was dissolved in propanol. The selectivity of the non-enzymatic UA sensor was determined with 0.1 mM interfering species, like urea, lactic acid, glucose, ascorbic acid, potassium ions, and sodium ions, in the presence of the same concentration of UA. The linear range of the UA sensor was determined by CV and chronoamperometry methods using various UA concentrations dissolved in 0.1 M phosphate buffer solution (PBS) at pH 7.0. Using this method, it was possible to estimate the low limit of detection of the non-enzymatic sensor [43].

3. Results and Discussion

3.1. Structural and Morphological Investigations of Radish White Peel Extract-Assisted Synthesis of $NiCo_2O_4$ Nanostructures

In Figure 1a, we show diffraction patterns measured by powder XRD on $NiCo_2O_4$ nanostructures that reveal their crystal quality. Furthermore, we investigated the effects of phytochemicals present in the white peel extract of radish on the crystal quality of $NiCo_2O_4$ nanostructures. The reference card number 00-020-0781 confirms that the typical reflections of $NiCo_2O_4$ nanostructures are well matched with the cubic phase of $NiCo_2O_4$. The diffraction patterns of $NiCo_2O_4$ nanostructures have been identified as (111), (220), (311), (222), (400), (511), and (440), respectively, at 19.40, 31.30, 36.880, 38.590, 44.850, 59.410, and 65.300. The morphology of $NiCo_2O_4$ nanostructures prepared with radish peel extract was examined by SEM. This was performed to compare them with pristine $NiCo_2O_4$ nanostructures, as shown in Figure 1b–f. $NiCo_2O_4$ nanostructures with a high degree of heterogeneity exhibit a typical nanorod-like orientation as shown in Figure 1b. Figure 1c–f illustrates that radish white peel extract altered the morphology of $NiCo_2O_4$ nanostructures toward short-range nanoparticles, confirming the influence of phytochemicals on surface modification. As well as being much smaller in size, nanostructures have a size range between 50 and 100 nm, which is characteristic of nanoparticles. Figure 1f illustrates that radish white peel extract significantly affects the size and morphology of $NiCo_2O_4$ nanostructures. According to Figure 1f, these phytochemicals determined the morphology and allowed the formation of aggregated and irregularly oriented nanostructures with unfavorable surface properties when 10 mL of radish white peel extract was used during the growth process. A phytochemical from radish white peel extract, shown in Scheme 1, contains oxygenated groups that provide ample coordination with nickel and cobalt metallic ions during the growth process, which results in morphological changes from nanorods to nanoparticles. As-prepared $NiCo_2O_4$ nanostructures were examined with HRTEM images and Fourier transform (FFT) patterns in order to analyze the deep morphological features and to calculate atomic d-spacing. Figure 2a illustrates that the nanoparticles were assembled in order to form a nanorod-like structure. The HRTEM image shown in Figure 2a confirms the excellent crystallinity of $NiCo_2O_4$ nanostructures. According to Figure 2b, pristine $NiCo_2O_4$ nanostructures have a d-spacing of 0.39 nanometers. Using elemental mapping. Figure 2b–d illustrates a uniform distribution of Ni, Co, and O. Figure 2e illustrates the EDS spectrum, which shows Co, Ni, and O as the primary elements. A TEM and HRTEM examination of $NiCo_2O_4$ nanostructures, as shown in Figure 3a, was conducted along with the calculation of d-spacing. A TEM image revealed typical nanoparticle morphologies, and HRTEM confirmed the high crystal quality of $NiCo_2O_4$ nanostructures (Figure 3). Figure 3a shows that $NiCo_2O_4$ nanostructures exhibit a spinel crystal structure and a cubic phase as revealed by the FFT analysis. According to Figure 3b–d, the d-spacing value of this sample was 0.36 nm, in agreement with results published for $NiCo_2O_4$ nanostructures. An elemental analysis of these nanostructures utilizing 5 mL of radish white peel extract revealed a homogeneous distribution of Co, Ni, and O elements. As shown in Figure 3e, the EDS spectrum indicates that the surface-modified $NiCo_2O_4$ nanostructures prepared using 5 mL of radish white peel extract contain quantified amounts of Ni, Co, and O.

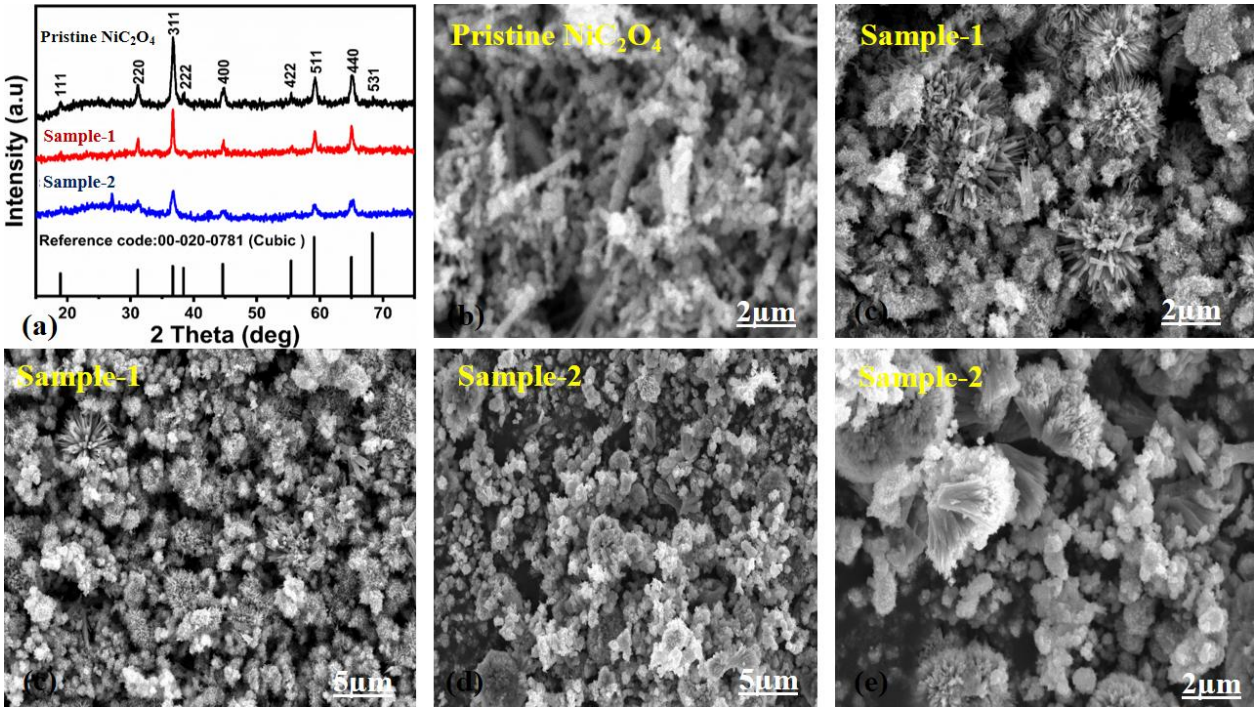

Figure 1. **(a)** Powder XRD diffraction patterns of pristine, 5 mL, and 10 mL of radish peel extract-assisted $NiCo_2O_4$ nanostructures, (b-f) Corresponding SEM images of (b) pristine, (c,d) 5 mL, and (e,f) 10 mL of radish peel extract-assisted $NiCo_2O_4$ nanostructures respectively

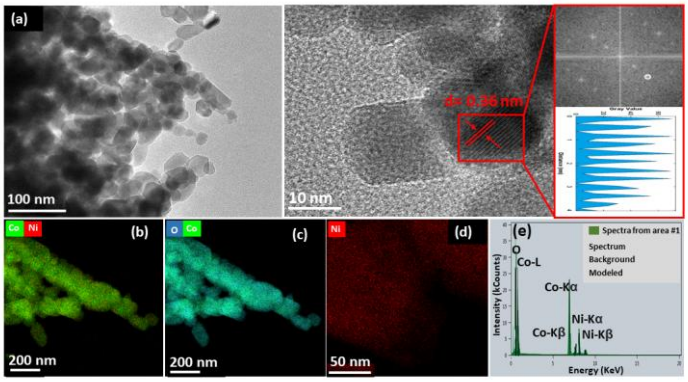

Figure 2. (**a**) TEM/HRTEM images of pristine $NiCo_2O_4$ nanostructures and FFT conversion at right side with d-spacing value; (**b–d**) corresponding elemental mapping of (**e**) EDS spectra of pristine $NiCo_2O_4$ nanostructures.

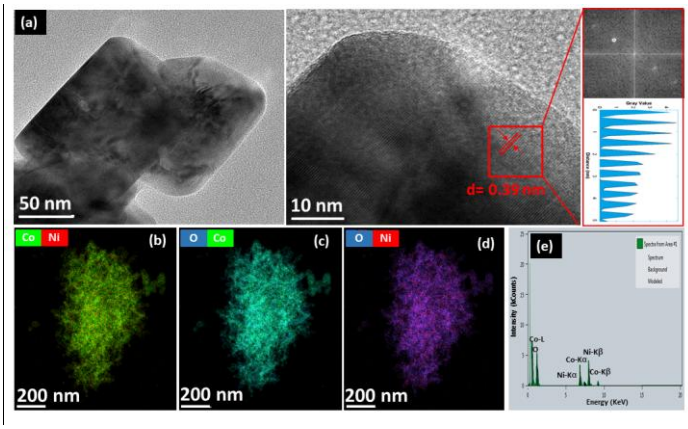

Figure 3. (**a**) TEM/HRTEM images of $NiCo_2O_4$ nanostructures prepared with 5 mL of radish white peel extract and FFT with d-spacing value on right-hand side; (**b**–**d**) elemental mapping of (**e**) EDS spectrum of $NiCo_2O_4$ nanostructures prepared with 5 mL of radish white peel extract.

The presence of green organic recuing, capping, and stabilizing agents in the radish white peel extract have the capability to tailor the surface properties of nanostructured materials [28,42]. Using XPS analysis, we were able to determine the chemical states and surface species of $NiCo_2O_4$ nanostructures both in the absence and presence of radish white peel extract, as shown in Figure 4. The XPS study has demonstrated a significant role of a wide range of green organic reducing, capping, and stabilizing agents on the surface chemical composition of $NiCo_2O_4$ nanostructures. To fit the XPS binding energies of each element, a standard carbon binding energy was used. Using pristine $NiCo_2O_4$ nanostructures as an example, Figure 4a illustrates the Co 2p spectrum, which indicates that there are two types of Co chemical states. According to Figure 5a, the estimated peaks at 779.47 eV and 780.54 eV correspond to the oxidation states of Co^{3+} and Co^{2+}, respectively. It is illustrated in Figure 5b how the Ni 2p spectrum can be fitted using Voigt's method. The fitted data consist of two spin orbital doublet peaks, 853.88 eV and 855.60 eV, corresponding to the Ni^{2+} and Ni^{3+} chemical states. It should be noted that despite these limitations, the shakeup peaks have been identified, and the data of Ni 2p fitted to XPS agree reasonably well with the reported peaks [36,44]. Furthermore, Figure 4c displays the O 1s spectrum for pristine $NiCo_2O_4$ nanostructures in addition to the metallic chemical states. The material surface shows three peaks at 529.69 eV, 531.10 eV, and 532.68 eV, respectively, corresponding to metal–oxygen chemical bonds, oxygen ions, and physic/chemisorbed water. Previous studies [36,44] have detected different oxygenated species on the surface of pristine $NiCo_2O_4$ nanostructures. The spectrum of O^{-1} s at 529.69 eV and 531.10 eV was correlated with the O^{2-} species present on $NiCo_2O_4$ nanostructures. A similar XPS analysis was conducted on $NiCo_2O_4$ nanostructures prepared in the presence of 5 mL of radish white peel extract as shown in Figure 4d–f. A large peak was observed in the spectrum of Co 2p associated with oxidation states, such as Co^{3+} and Co^{2+}, at 779.57 eV and 781.12V, respectively. By contrast, Ni^{2+} and Ni^{3+} were observed at 853.96 eV and 855.61 eV, respectively. Furthermore, three contributions were observed in the O1s spectrum at 529.67 eV, 531.16 eV, and 533.42 eV, corresponding to the metal–oxygen bonds, oxygen ions (O_2), and physic/chemisorbed water on the surface of the material. The XPS study has revealed that green organic reducing, capping, and stabilizing agents from radish white peel extract have a relatively high concentration of oxygen ions (O^-) and Co^{3+} compared to pristine $NiCo_2O_4$ nanostructures. These surface properties are highly desirable for a catalytic reaction [36,44]. Furthermore, the green organic reducing, capping, and stabilizing agents have induced a high abundance of Co^{3+}/Co^{2+} and Ni^{2+}/Ni^{3+} metallic positively charged ions in the surface of $NiCo_2O_4$ nanostructures. Consequently, these metallic ions have offered a high density of catalytic sites for the favorable electrocatalytic reaction of UA.

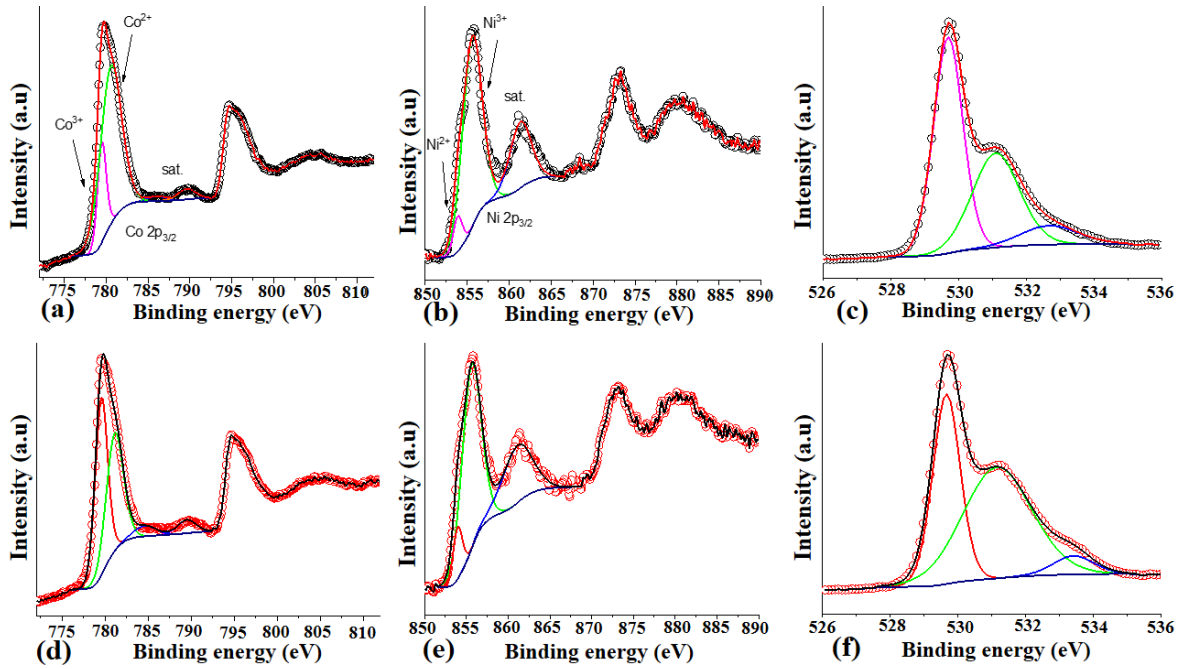

Figure 4. XPS-resolved Co 2p, Ni 2p, O1s spectra for pristine (**a**–**c**) and (**d**–**f**) XPS-resolved Co 2p, Ni 2p, O1s of 5 mL of radish peel extract-assisted $NiCo_2O_4$ nanostructures.

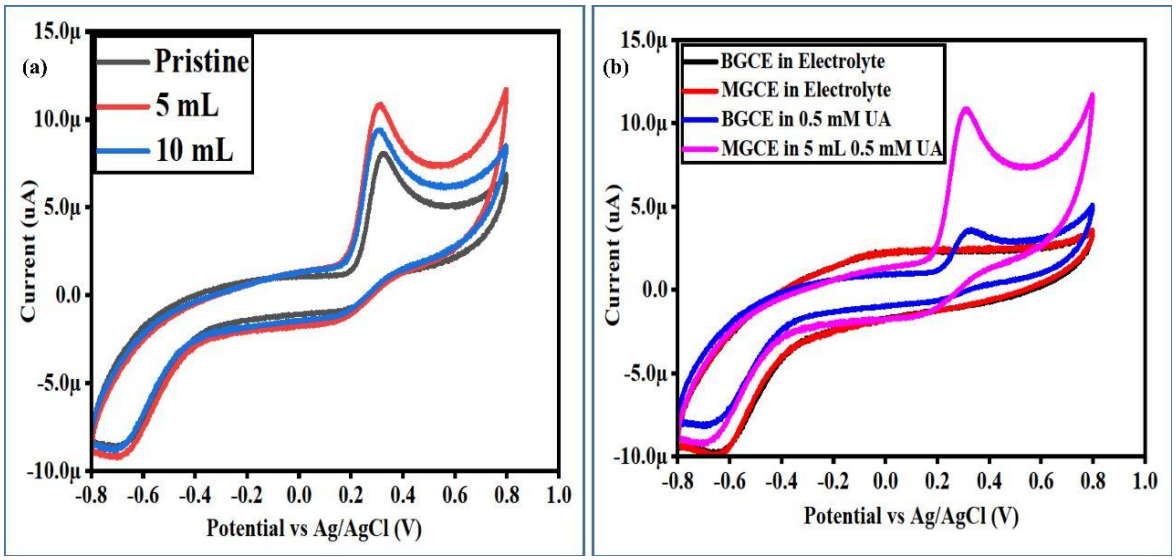

Figure– 5. (**a**) Cyclic voltammograms at a scan rate of 50 mV/s of MGCE with 5 mL and 10 mL of radish white peel extract-assisted $NiCo_2O_4$ and pristine $NiCo_2O_4$-modified GCE in the presence of 0.5 mM of UA in 0.1 M PBS pH 7.0. (**b**) Cyclic voltammograms at 50 mV/s of bare GCE and modified with 5 mL of assisted $NiCo_2O_4$ in electrolyte and equal in the presence of 0.5 mM UA in 0.1 M PBS pH 7.0.

3.2. Non-Enzymatic Uric Acid (UA) Oxidation on the Surface-Modified $NiCo_2O_4$ Nanostructures with Radish White Peel Extract

$NiCo_2O_4$ nanostructures were characterized electrochemically using a three-electrode cell configuration in order to detect UA. Figure 5a illustrates preliminary studies conducted with cyclic voltammetry to identify the most efficient $NiCo_2O_4$ nanostructures for the oxidation of UA. A CV curve was measured at 50 mV/s using both pristine $NiCo_2O_4$ nanostructures and $NiCo_2O_4$ nanostructures, which had been surface-modified with 5 mL and 10 mL of radish white peel extract in the absence or presence of UA. A CV curve, such as that shown in Figure 6a, is representative of electrochemical catalytic signals obtained from pristine and surface-modified $NiCo_2O_4$ nanostructures placed in 0.5 mM UA in a phosphate buffer solution at pH 7.0. When comparing $NiCo_2O_4$ nanostructures prepared with 5 mL of radish white peel extract with pristine and surface-modified $NiCo_2O_4$ nanostructures soaked in 10 mL of radish white peel extract, it is evident that the electrocatalytic properties of these nanostructures are well described when compared to pristine and surface-modified $NiCo_2O_4$ nanostructures soaked in 10 mL of radish white peel extract. This is due to the enhanced conductivity of the material and the enriched surface sites on the surface. Due to the poor catalytic properties and the electrical conductivity of $NiCo_2O_4$, the CV curve shows that the peak current is relatively low when UA is oxidized on pristine $NiCo_2O_4$ nanostructures. However, the electrochemical performance of $NiCo_2O_4$ nanostructures was strongly dependent on the volume of radish white peel extract, as evidenced by the limited electrochemical signal in Figure 5a for a sample containing 10 mL of radish white peel extract. For the large-scale synthesis of $NiCo_2O_4$ nanostructures that are highly desirable for electrochemical applications, 5mL of radish white peel extract appears to provide the best conditions. Moreover, $NiCo_2O_4$ nanostructures prepared using 5 mL of radish white peel extract and bare glassy carbon electrodes were tested in the presence of 0.5 mM UA and only in the presence of a phosphate buffer solution at pH 7.0, as shown in Figure 6b. UA is believed to cause the signal to originate primarily from $NiCo_2O_4$ nanostructures; however, the bare glassy carbon electrode, as shown in Figure 5b, did not demonstrate any electrochemical signal for either the electrolyte or analyte. Based on the CV analysis, $NiCo_2O_4$ nanostructures synthesized with radish white peel extract were only effective for driving UA oxidation in the phosphate buffer solution, thus full non-enzymatic UA sensor characterization was carried out.

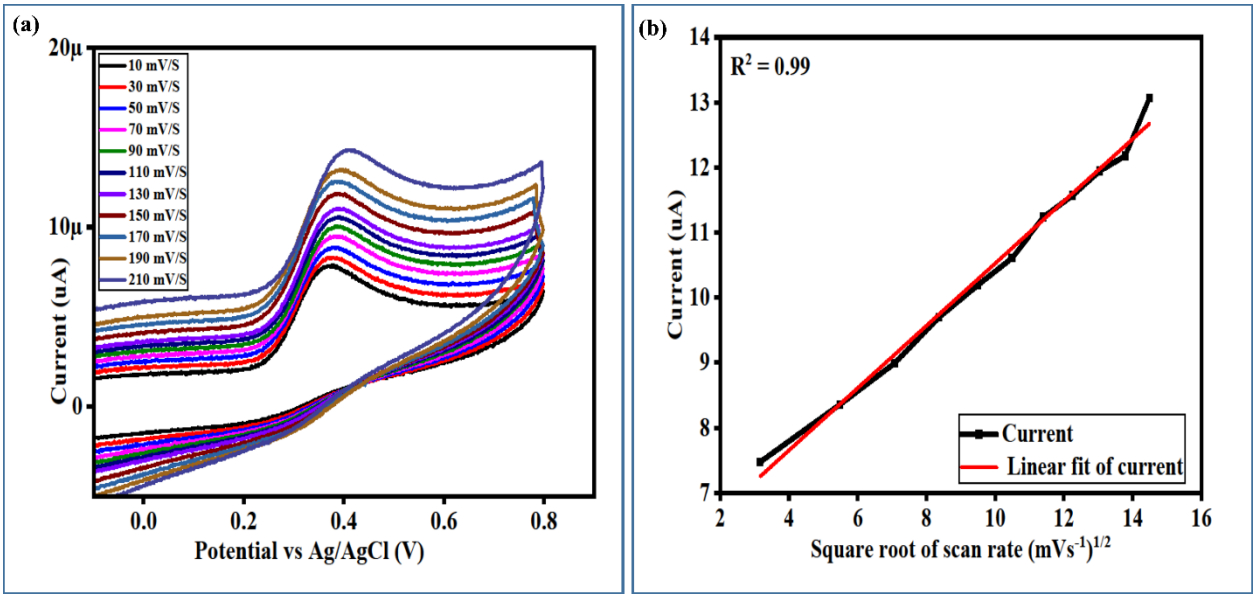

Figure– 6. (**a**) Cyclic voltammograms at a scan rate of 50 mV/s of MGCE with 5 mL of radish white peel extract-assisted $NiCo_2O_4$-modified GCE in the presence of 0.5 mM of UA in 0.1 M PBS pH 7.0. (**b**) Linear plot of peak current against square root of scan rate.

When UA is oxidized on $NiCo_2O_4$ nanostructures, electrons are transferred from UA to Co^{3+} and Ni^{3+} ions and reduced to Co^{2+} and Ni^{2+}. In addition to altering the size and surface properties of $NiCo_2O_4$ nanostructures, phytochemicals in radish white peel extract enhanced the charge transfer between the electrode and analyte solution. Figure 6a shows the electrode kinetics at various scan rates using CV analysis in a solution containing 0.5 mM UA. It is evident from this example that increasing scan rates linearly increase peak current. This confirms the diffusion-controlled processing of the modified GCE with $NiCo_2O_4$. As shown in Figure 6b, a linear plot was obtained by plotting the peak current against the square root of the scan rate. The purpose of this was to simplify the understanding of electrode kinetics. $NiCo_2O_4$ nanostructure-based electrodes have been found to have a high scan rate in recent studies. According to CV analysis, UA oxidation is accompanied by two electron and proton transfers [44–47]. Also, the observed regression coefficient value (R^2—0.99) supports the analytical aspects of an enzyme-free UA sensor for precise and accurate quantification of UA. Therefore, surface adsorption and electrochemistry were responsible for controlling the UA oxidation reaction.

Our study examined the effect of pH on the oxidation process of $NiCo_2O_4$ nanostructures prepared with 5 mL of radish white peel extract. As a result of the pH change of 0.5 mM of UA, CV curves for $NiCo_2O_4$ nanostructures are illustrated in Figure 7a. We evaluated UA sensor performance at pH 7.0 based on the shape and current of the peak, which were more apparent at this pH level. A pH study indicated that $NiCo_2O_4$ nanostructures are strongly regulated by the pH of the analyte solution when it comes to their activity. Such aspects have previously been examined in a study [48]. $NiCo_2O_4$ nanostructures are limited in their ability to function under different pH conditions of analyte solutions. Consequently, the catalytic sites are diminishing, the material is unstable, and the surfaces are etched [49]. As a result of this experiment, the pH of the UA solution was varied between 6.0, 7.0, 8.0, and 9.0. As a result, CV displayed a stable response at pH 7.0, and all electrochemical measurements were made at this pH level. To facilitate interpretation of CV curves, a line plot was also made of the effect of pH on the UA solution. Figure 7b illustrates that pH 7.0 resulted in the highest peak current, which improved charge transfer and increased the $NiCo_2O_4$ nanostructures' electrochemical activity. UA oxidation occurs when two protons are lost and is suppressed by UA's low pH of 7.0. However, at higher pH levels, $NiCo_2O_4$ nanostructures are likely to be etched, resulting in poor performance.

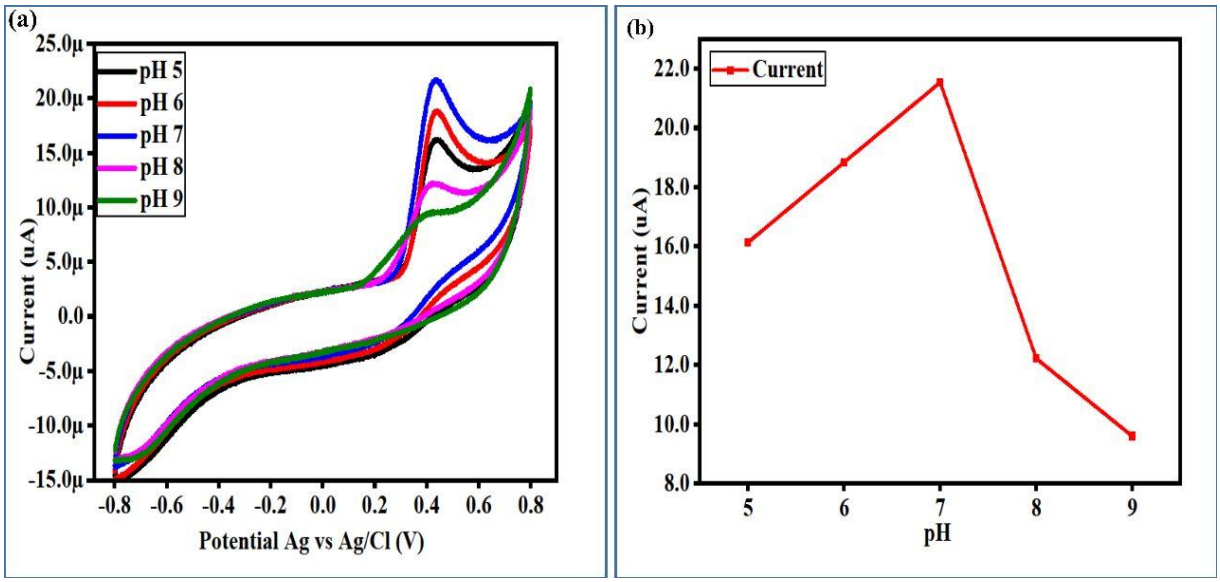

Figure –7. (**a**) Cyclic voltammograms at a scan rate of 50 mV/s of MGCE with 5 mL of radish white peel extract-assisted $NiCo_2O_4$-modified GCE in the presence of different pH values of 0.5 mM of UA in 0.1 M PBS. (**b**) Linear plot of peak current versus different pH values of 0.5 mM of UA in 0.1 M PBS.

3.3. The Calibration Plots, Stability, Repeatability, and Selectivity Studies of a Newly Developed Non-Enzymatic UA Sensor Based on Surface-Modified $NiCo_2O_4$ Nanostructures

Analyses of the linear range and limit of detection of UA were conducted using $NiCo_2O_4$ nanostructures prepared with 5 mL of radish white peel extract. The linear range of a non-enzymatic UA sensor was evaluated by varying electrochemical modes in order to maintain the sensing range of each electrochemical mode. The linear range of UA was first investigated by CV at 50 mV/s in a phosphate buffer solution at pH 7.0 at different concentrations of UA. The linear range of UA was determined to be between 0.1 mM and 8 mM, and the peak current for UA oxidation increased linearly with increasing UA concentration, as shown in Figure 8a. Based on this study, it can be concluded that UA non-enzymatic sensors have demonstrated a wide linear range to date [13,50–56] as well as the low detection limit of 0.005 mM, indicating a high degree of applicability for the monitoring of UA at either low or high concentrations in real samples. In addition, the linear plot shown in Figure 8b was calculated by selecting the oxidation peak current for each UA concentration against the UA concentration in order to determine the accuracy and precision of a newly developed non-enzymatic UA sensor. It appears that UA sensors have the ability to monitor a wide range of UA concentrations from practical samples based on the linear plot of the CV results. On the basis of the methods reported in the literature, a limit of detection (LOD) and a limit of quantification (LOQ) were estimated [56]. In this study, the LOD and LOQ were determined to be 0.005 mM and 0.008 mM, respectively. Table 1 compares the wide linear range of UA detection and the low LOD of the non-enzymatic UA sensors presented with the existing UA biosensors. Following the analysis of the comparisons, it became evident that the proposed method can be of great interest as an alternative method for the detection of UA in real samples, where a wide linear range and a low limit of detection are desired. Additionally, linear sweep voltammetry (LSV) mode was used to estimate the calibration of the newly developed non-enzymatic UA sensor, and Figure 9a illustrates the range of UA detection obtained. Figure 9a illustrates that the proposed UA sensor configuration is capable of detecting UA over a wide linear range from 0.1 mM to 7.0 mM and producing a significant amount of current. When UA concentration increases in LSV measurements, there is a higher current generated, which indicates that the newly developed UA sensor is highly sensitive. Besides the LSV measurements, we also made a linear plot of peak current and UA concentrations (Figure 9b). The linear fitting of LSV curves reveals that the proposed non-enzymatic UA sensor has excellent analytical performance, as indicated by its regression coefficient value of 0.99. Based on full CV curves and half CV curves from LSV, the present UA sensor is capable of detecting a wide linear range of UA with precision and accuracy. Additionally, the linear range for another highly sensitive electrochemical mode of amperometry at 0.3 V was used to determine the linear range of the UA sensor. Figure 10a illustrates this range for various UA concentrations detected. UA concentrations between 0.1 and 6 mM were highly sensitive to the amperometric signal. Figure 10b illustrates a linear plot of the amperometric signal for these different concentrations of UA.

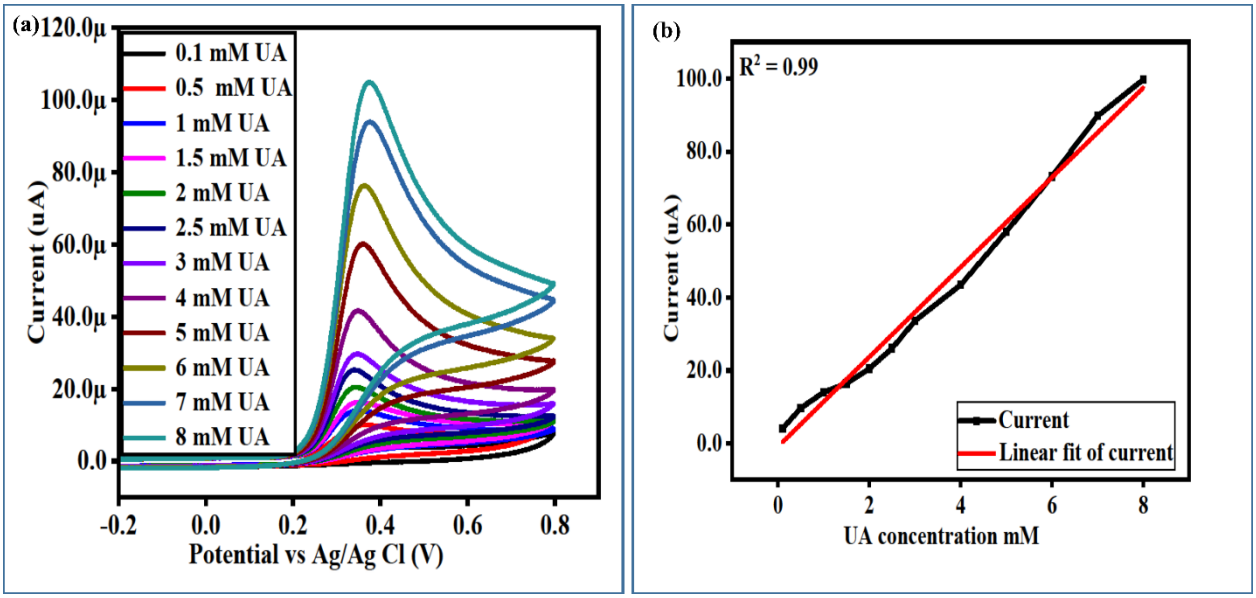

Figure –8. Cyclic voltammograms at a scan rate of 50 mV/s of MGCE with 5 mL of radish white peel extract-assisted $NiCo_2O_4$ in the presence of various concentrations of UA in 0.1 M PBS pH 7.0. (**b**) Linear plot of peak current versus successive increase in UA concentrations.

Table 1. Performance comparison of the enzyme-free sensor based on $NiCo_2O_4$ nanostructures grown with 5 mL radish (*Raphanus sativus*) extract versus several non-enzymatic UA sensors in the literature.

Sensing Electrode Material	Linear Range (μM)	Detection of Limit (μM)	References
PCN [a]/MWCNT [b]	0.2–20	0.139	[50]
B-MWCNTS [c]	62–250	0.65	[51]
Pd/RGO [d]	6–469.5	1.6	[18]
Au/RGO [d]	8.8–53	1.8	[52]
PtNi@MoS_2 [e]	0.5–600	0.1	[53]
Cysteic acid	1.0–19	0.36	[54]
Co_3O_4	500–3500	100	[56
PANI-Pt NPs/GCE	70–1000	1	[59]
MWNTs/MGF	300–1000	0.93	[55]
$NiCo_2O_4$ (30%)/Nano-ZSM-5	0.9–1000	0.7	[60]
Fe_2O_3@Au	100–10,000	0.087	[56]
$NiCo_2O_4$ NPs	100–8000	0.005	This work

[a] Porous g-C_3N_4. [b] Multi-walled carbon nanotubes. [c] Boron-dopped multi-walled carbon naotubes. [d] Reduced graphene oxide. [e] PtNi bimetallic nanoparticles-loaded nanosheets.

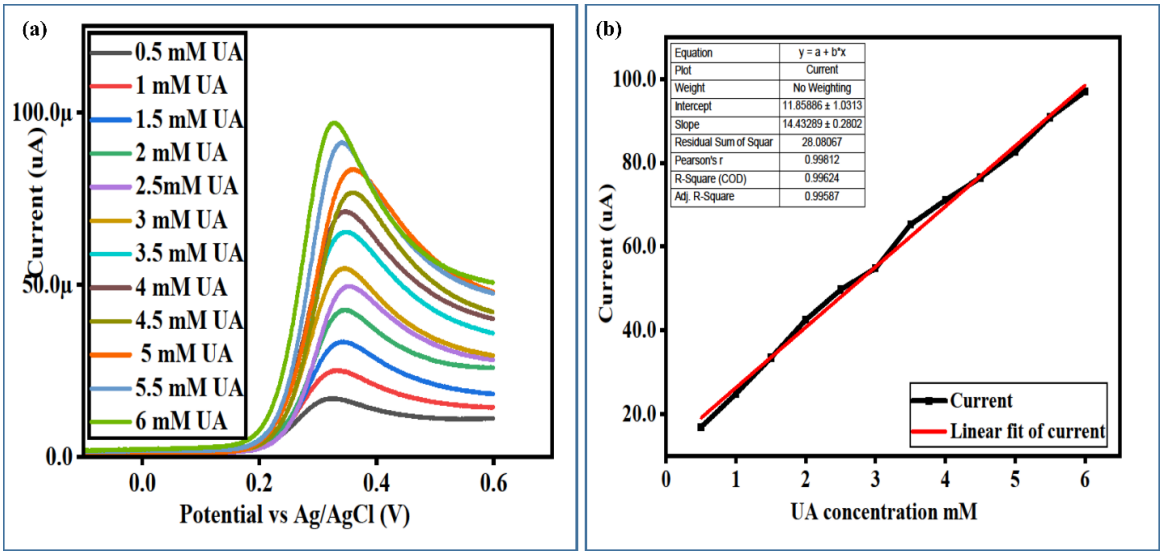

Figure– 9. (**a**) Linear sweep voltammetry at a scan rate of 10 mV/s of MGCE with 5 mL of radish white peel extract-assisted $NiCo_2O_4$ in the presence of various concentrations of UA in 0.1 M PBS pH 7.0. (**b**) Linear plot of peak current versus successive increase in UA concentrations.

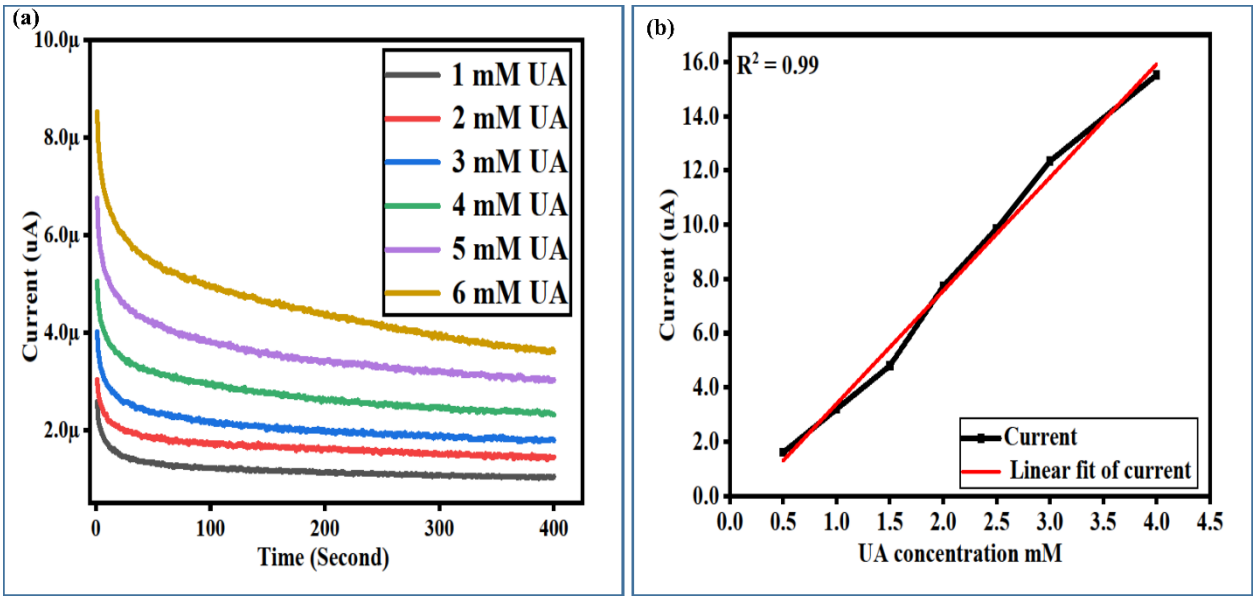

Figure –10. (**a**) Chronoamperometric response curves measured at an applied potential of 0.3 V of MGCE with 5 mL of radish white peel extract-assisted $NiCo_2O_4$ in the presence of various concentrations of UA in 0.1 M PBS pH 7.0. (**b**) Linear plot of peak current versus successive increase in UA concentrations.

A linear fitting of the UA detection resulted in excellent performance with strong analytical features. The results confirm the algorithm's promising performance for the detection of UAs and its application in real-world sample analysis. Due to the high density of catalytic sites, enhanced electrical conductivity, and biomimetic compatibility of nanostructured material with the surface of GCE, UA detection on surface-modified $NiCo_2O_4$ nanostructures with radish white peel extract presented outstanding linearity and high sensitivity. The SEM, XRD, HRTEM, and XPS measurements demonstrated tailored morphology, excellent crystal quality, a significant amount of surface vacancies, and an abundance of Co(III) and Ni(II) chemical states, which led to the superior performance of $NiCo_2O_4$ nanostructures prepared with 5 mL of radish white peel extract. In order to evaluate the selectivity of a UA sensor before implementing it in actual sample analysis, we tested the proposed UA sensor in the presence of possible interfering species

during detection of UA in real blood and urine samples. It was determined that the selectivity of the interfering compounds could be monitored by preparing $NiCo_2O_4$ nanostructures with radish white peel extract containing glucose, ascorbic acid, urea, lactic acid, mannose, sodium ions, chloride ions, potassium ions, and calcium ions, as shown in Figure 11. CV curves were measured following the sequential addition of interfering species to a solution of 0.5 mM UA. Based on Figure 11a, the interfering species had the same concentration as the UA. As a result of the sequential addition of interfering species in the presence of UA, UA was not affected in terms of oxidation peak position, drift in oxidation potential, and peak current, suggesting that the proposed UA sensor configuration has excellent selectivity and is suitable for the detection of UA in biological matrixes. In order to better visualize the variation in UA peak current after the addition of interfering species, a bar graph of the peak current was plotted. The change in peak current could be seen at less than 4%, as shown in Figure 11b. The excellent selectivity of the proposed UA sensor can be attributed to the surface modification of $NiCo_2O_4$ nanostructures with phytochemicals from radish white peel extract, which enabled it to detect specific electroactive molecules.

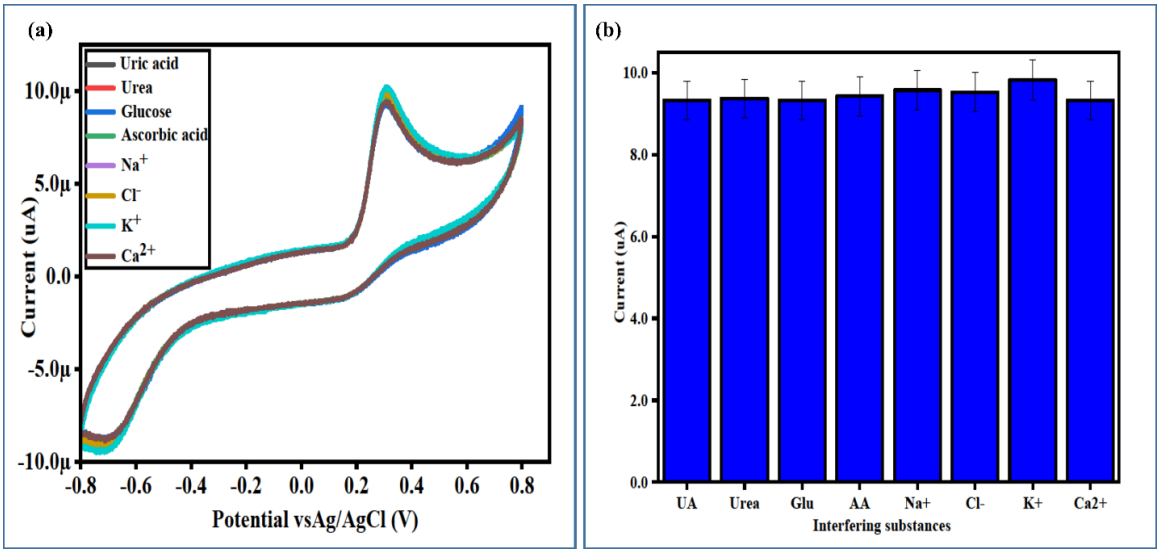

Figure– 11. (**a**) Cyclic voltammograms at a scan rate of 50 mV/s of MGCE with 5 mL of radish white peel extract-assisted $NiCo_2O_4$ in the presence of 0.5 mM UA and other competing interfering agents in 0.1 M PBS pH 7.0; (**b**) bar graph of peak current with addition of interfering species for the illustration of the variation of the peak current.

We examined the repeatability of the modified UA sensor electrode by measuring 20 CV cycles at a scan rate of 50 mV/s in 0.5 mM. It was found that the device could be reused, as shown in Figure 12a. The long-term stability of UA biosensors is always a challenge, especially for enzymatic biosensors, thus we have designed a non-enzymatic UA sensor with potential application in real analysis. This is evident from the bar graph of peak current after several repeatable CV cycles as shown in Figure 12b. An error of less than 5% indicates the excellent analytical features of the method. A non-enzymatic UA based on surface-modified $NiCo_2O_4$ nanostructures can be used for long-term applications, since the material does not change surface features under ambient conditions. However, we examined the stability of $NiCo_2O_4$ nanostructures in 0.5 mM UA solution by measuring the amperometric response over a period of 1000 s. This is depicted in Figure 13a. According to the response time, the present UA sensor did not exhibit any current fluctuation for the selected time. Therefore, it is suitable for long-term applications.

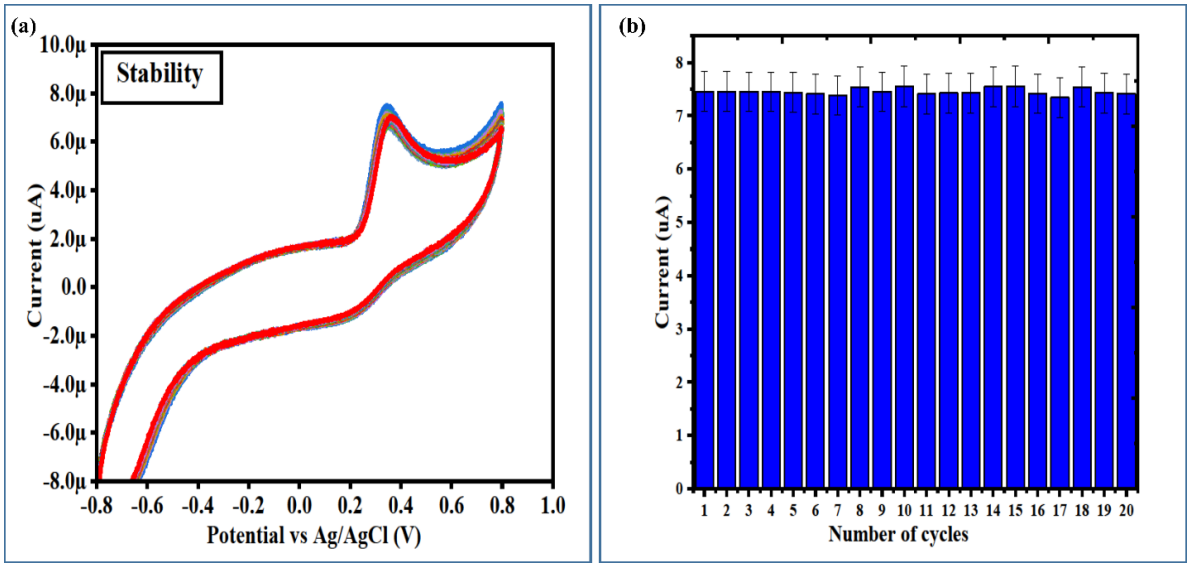

Figure –12. Cyclic voltammograms at a scan rate of 50 mV/s of MGCE with 5 mL of radish white peel extract-assisted $NiCo_2O_4$ in the presence of 0.5 mM UA in 0.1 M PBS pH 7.0; (**b**) bar graph of peak current for the description of change in the peak current with increasing number of CV cycles. Linear plot of peak current versus successive increase in UA concentrations.

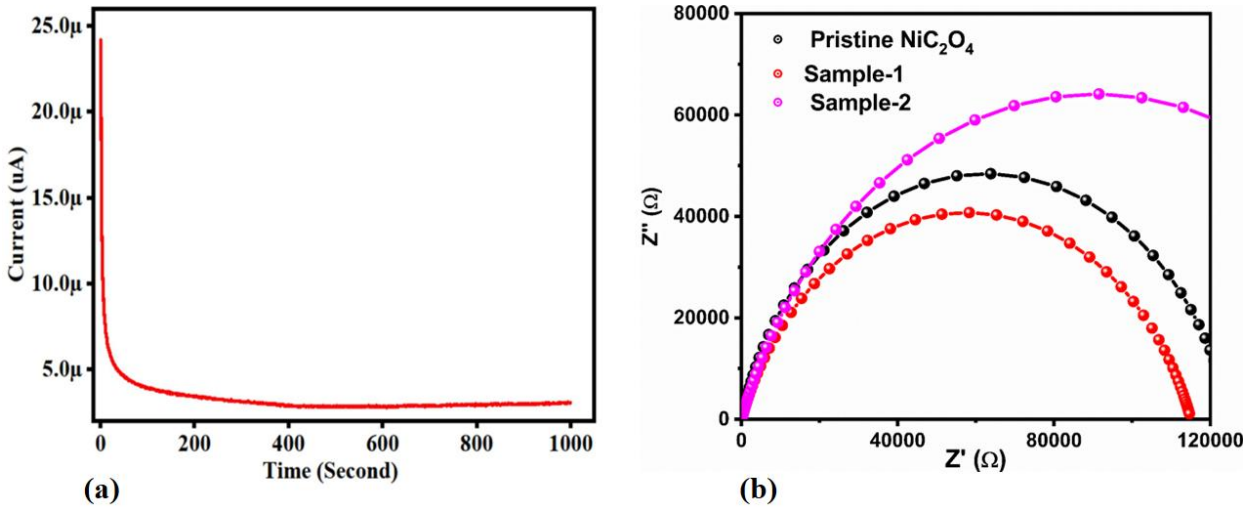

Figure– 13. (**a**) Chronoamperometric response of MGCE with 5 mL of radish white peel extract-assisted $NiCo_2O_4$ in 0.5 mM prepared in 0.1 M PBS pH 7.0 for the demonstration of stability of modified electrode; (**b**) EIS Nyquist plots collected for the MGCE with pristine, 5 mL, and 10 mL of radish white peel extract-assisted $NiCo_2O_4$ in 0.5 mM UA using frequency range of 100 kHz to 1 Hz, amplitude of 10 mV, and biasing potential of 0.6 V.

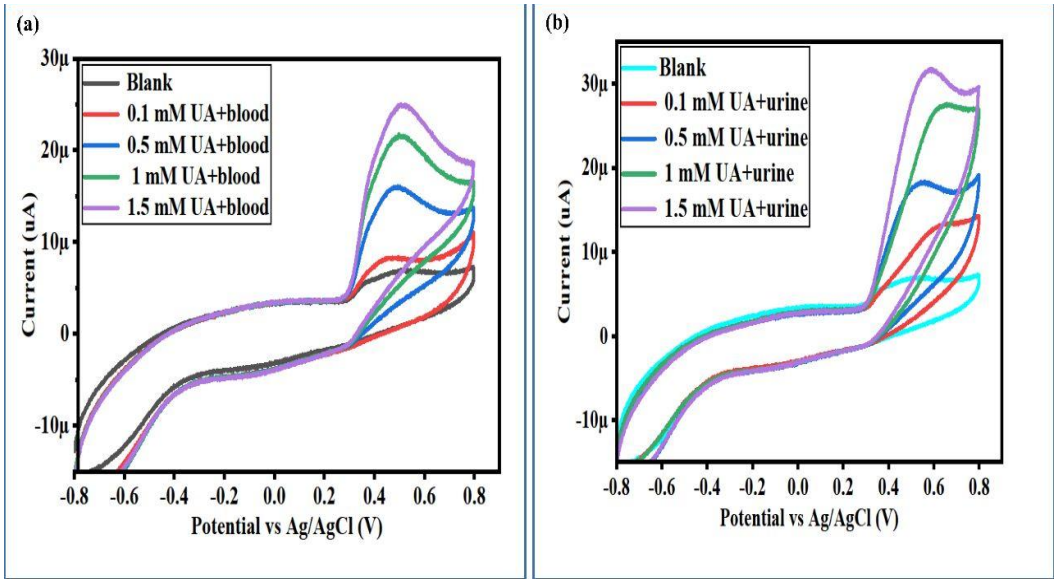

Fig –14. (a) Cyclic voltammograms at a scan rate of 50 mV/s of MGCE with 5 mL of radish white peel extract assisted $NiCo_2O_4$ for the quantitation of UA form diluted human blood real samples in 0.1M PBS pH 7.0 and successive addition method , (b) Cyclic voltammograms at a scan rate of 50 mV/s of MGCE with 5 mL of radish white peel extract assisted $NiCo_2O_4$ for the quantitation of UA form diluted human urine real samples in 0.1M PBS pH 7.0 and successive addition method.

Our results in terms of wide linear range, low limit of detection, excellent selectivity, stability, and repeatability confirmed the superior performance compared to other UA sensors/biosensors reported in the existing literature, as shown in Table 1. To support the electrochemical performance of the prepared $NiCo_2O_4$ nanostructures, electrochemical impedance spectroscopy (EIS) was performed using a sweeping frequency range of 100 kHz to 1 Hz, amplitude of 10 mV and biasing potential of 0.6 V. The Nyquist plots were measured for the three samples of $NiCo_2O_4$ nanostructures, including pristine sample 1 and sample 2 in 0.5mM UA, and the EIS data were fitted with Z-view software as illustrated in Figure 13b. The intercept of the semicircle of Nyquist plots at high frequency represents electrolyte resistance. The arc of the Nyquist plots indicates the charge transport between the working electrode based on $NiCo_2O_4$ nanostructures and the 0.5mM analyte solution [60]. The estimated values of charge-transfer Rct for pristine $NiCo_2O_4$ nanostructures, sample 1, and sample 2 in the presence of analyte were as 125,100 Ohm, 114970 Ohm, and 181,270 Ohm, respectively. The EIS study has verified that sample 1 of $NiCo_2O_4$ nanostructures prepared with 5 mL of radish white peel extract has more favorable charge transport over the pristine and sample 2-based $NiCo_2O_4$ nanostructures; hence, we observed better electrochemical measurements of sample 1 toward the quantification of a sensitive UA signal.

3.4. Human Blood Sample Analytical Applications of Proposed Non-Enzymatic UA Sensor-Based $NiCo_2O_4$ Nanostructures

The non-enzymatic UA sensor configuration presented in Figure 14a,b has been evaluated on real human blood samples. A healthy volunteer and a high UA patient provided blood samples with their own consent. The samples were diluted 30 times with 0.1 M phosphate buffer solution of pH 7.0 and used directly during the setup of three electrode cells for electrochemical quantification of UA. UA non-enzymatic sensor performance confirms its potential applicability and reliability for the quantification of UA from biological fluids, and even food products with high probability, as shown in Table 2. A percent relative standard deviation RSD (%) was calculated from the sum of (standard deviation/mean of quantified UA concentration data using three repeated experiments for UA detection) × 100%.

Table 2. Real sample analysis of UA from various blood samples (Blood 1 = healthy blood sample; Blood 2 = high-level UA patient).

Sample	Added (mM)	Found (mM)	%Recovery	% RSD
Blood 1	-	0.1	-	
-	0.5	0.612 ± 0.002	101.66	0.52
-	1	1.123 ± 0.0023	101.81	0.53
-	2	2.084 ± 0.0017	99	0.49
-	2.5	2.621 ± 0.0013	100.77	0.54
Blood 2	-	1.00	-	-
-	1.5	2.533 ± 0.0022	101.2	0.48
-	2	3.082 ± 0.0019	102.66	0.56
-	2.5	3.514 ± 0.0024	100.28	0.50
-	3	4.063 ± 0.0018	101.5	0.53

4. Conclusions

An easy and rapid method has been developed for quantifying UA in human blood and urine samples by using surface-modified $NiCo_2O_4$ nanostructures. It has been combined with phytochemicals derived from radish white peel. It was determined that a volume of 5 mL of radish white peel extract was optimal for the large-scale synthesis of $NiCo_2O_4$ nanostructures. The CV exhibited a linear range from 0.1 mM to 8 mM, the LSV showed 0.1 mM to 7 mM, and the amperometric signal for the UA sensor showed a linear range from 0.1 mM to 4 mM. We found that the LOD and LOQ of the present non-enzymatic UA sensor were 0.005 mM and 0.008 mM, respectively. Furthermore, the present UA sensor was evaluated in terms of its selectivity, stability, repeatability, and sensitivity. Consequently, a wide linear range and a low limit of detection were achieved. Several factors contribute to the sensor's performance, including large surface vacancies, abundant chemical states of Co(III), Ni(II), tailored surface morphology, fast charge-transfer rate, and outstanding crystal quality. It has been demonstrated that there is a satisfactory level of detection of UA in human blood samples (healthy and UA patients).

Author Contributions: A.G.S. performed material synthesis and partial electrochemical measurements; A.T. performed XRD analysis and measurement; B.W. performed the real sample analysis; A.S.C. performed the partial electrochemical measurement and analyzed the obtained results; T.P. performed the partial supervisions and preview the obtained results; A.N. performed validation of results and proofread the paper; E.A.D. performed SEM analysis; L.M.A.S. performed EIS study; M.P. performed HRTEM analysis; A.H.I. performed overall review of the obtained results; K.L. performed XPS and HRTEM measurement; B.V. performed XPS analysis and proofread the structural results; Z.H.I. performed main supervision and wrote the first draft of manuscript. All authors have read and agreed to the published version of the manuscript.

Funding: Not Applicable

Institutional Review Board Statement: Not Applicable

Informed Consent Statement: Informed consent was obtained from all subjects involved in the study

Data Availability Statement: The authors declare that the data supporting the findings of this study are available within the paper

Acknowledgments: The authors would like to gratefully acknowledge the Higher Education Commission Pakistan for partial support under the project NRPU/8350. We also extend our sincere appreciation to the Researchers Supporting Project Number (RSP2023R79) at King Saud University, Riyadh, Saudi Arabia. Brigitte Vigolo would like to thank the platform "Microscopies, Microprobes and Metallography (3 M)" (Institut Jean Lamour, IJL, Nancy, France) for access to SEM facilities

and F. Alnjiman for his valuable help. Authors would also like to acknowledge partial funding of the Ajman University, Grant ID: DRGS ref. 2022-IRG-HBS-5.

Conflicts of Interest: Authors declare no competing interests in the presented research work.

References

1. Martinon, F. Mechanisms of uric acid crystal-mediated autoinflammation. *Immunol. Rev.* **2010**, *233*, 218–232.
2. Hu, F.X.; Hu, T.; Chen, S.; Wang, D.; Rao, Q.; Liu, Y.; Dai, F.; Guo, C.; Yang, H.B.; Li, C.M. Single-atom cobalt-based electrochemical biomimetic uric acid sensor with wide linear range and ultralow detection limit. *Nano-Micro Lett.* **2021**, *13*, 1–13.
3. Qu, S.; Li, Z.; Jia, Q. Detection of purine metabolite uric acid with picolinic-acid-functionalized metal–organic frameworks. *ACS Appl. Mater. Interfaces* **2019**, *11*, 34196–34202.
4. Feig, D.I.; Kang, D.-H.; Johnson, R.J. Uric acid and cardiovascular risk. *N. Engl. J. Med.* **2008**, *359*, 1811–1821.
5. Palmer, I.; Schutte, A.; Huisman, H. Uric acid and the cardiovascular profile of African and Caucasian men. *J. Hum. Hypertens.* **2010**, *24*, 639–645.
6. Roberts, J.M.; Gammill, H.S. Preeclampsia: Recent insights. *Hypertension* **2005**, *46*, 1243–1249.
7. Dey, N.; Bhattacharya, S. Nanomolar level detection of uric acid in blood serum and pest-infested grain samples by an amphiphilic probe. *Anal. Chem.* **2017**, *89*, 10376–10383.
8. Talaat, K.M.; El-Sheikh, A.R. The effect of mild hyperuricemia on urinary transforming growth factor beta and the progression of chronic kidney disease. *Am. J. Nephrol.* **2007**, *27*, 435–440.
9. Chen, X.; Chen, J.; Wang, F.; Xiang, X.; Luo, M.; Ji, X.; He, Z. Determination of glucose and uric acid with bienzyme colorimetry on microfluidic paper-based analysis devices. *Biosens. Bioelectron.* **2012**, *35*, 363–368.
10. Pormsila, W.; Krähenbühl, S.; Hauser, P.C. Capillary electrophoresis with contactless conductivity detection for uric acid determination in biological fluids. *Anal. Chim. Acta* **2009**, *636*, 224–228.
11. Westley, C.; Xu, Y.; Thilaganathan, B.; Carnell, A.J.; Turner, N.J.; Goodacre, R. Absolute quantification of uric acid in human urine using surface enhanced Raman scattering with the standard addition method. *Anal. Chem.* **2017**, *89*, 2472–2477.
12. Rebelo, I.A.; Piedade, J.A.P.; Oliveira-Brett, A.M. Development of an HPLC method with electrochemical detection of femtomoles of 8-oxo-7, 8-dihydroguanine and 8-oxo-7, 8-dihydro-2′-deoxyguanosine in the presence of uric acid. *Talanta* **2004**, *63*, 323–331.
13. Wang, C.; Yuan, R.; Chai, Y.; Chen, S.; Hu, F.; Zhang, M. Simultaneous determination of ascorbic acid, dopamine, uric acid and tryptophan on gold nanoparticles/overoxidized-polyimidazole composite modified glassy carbon electrode. *Anal. Chim. Acta* **2012**, *741*, 15–20.
14. Lian, X.; Yan, B. Phosphonate MOFs composite as off–on fluorescent sensor for detecting purine metabolite uric acid and diagnosing hyperuricuria. *Inorg. Chem.* **2017**, *56*, 6802–6808.
15. Yao, D.; Vlessidis, A.G.; Evmiridis, N.P. Microdialysis sampling and monitoring of uric acid in vivo by a chemiluminescence reaction and an enzyme on immobilized chitosan support membrane. *Anal. Chim. Acta* **2003**, *478*, 23–30.
16. Yang, X.; Kirsch, J.; Simonian, A. Campylobacter spp. detection in the 21st century: A review of the recent achievements in biosensor development. *J. Microbiol. Methods* **2013**, *95*, 48–56.
17. Yang, X.; Kirsch, J.; Olsen, E.V.; Fergus, J.W.; Simonian, A.L. Anti-fouling PEDOT: PSS modification on glassy carbon electrodes for continuous monitoring of tricresyl phosphate. *Sens. Actuators B Chem.* **2013**, *177*, 659–667.
18. Wang, J.; Yang, B.; Zhong, J.; Yan, B.; Zhang, K.; Zhai, C.; Shiraishi, Y.; Du, Y.; Yang, P. Dopamine and uric acid electrochemical sensor based on a glassy carbon electrode modified with cubic Pd and reduced graphene oxide nanocomposite. *J. Colloid Interface Sci.* **2017**, *497*, 172–180.
19. Sha, R.; Puttapati, S.K.; Srikanth, V.V.; Badhulika, S. Ultra-sensitive non-enzymatic ethanol sensor based on reduced graphene oxide-zinc oxide composite modified electrode. *IEEE Sens. J.* **2017**, *18*, 1844–1848.
20. Sha, R.; Badhulika, S. Facile green synthesis of reduced graphene oxide/tin oxide composite for highly selective and ultra-sensitive detection of ascorbic acid. *J. Electroanal. Chem.* **2018**, *816*, 30–37.
21. Sha, R.; Komori, K.; Badhulika, S. Graphene–Polyaniline composite based ultra-sensitive electrochemical sensor for non-enzymatic detection of urea. *Electrochim. Acta* **2017**, *233*, 44–51.
22. Ndamanisha, J.C.; Guo, L. Electrochemical determination of uric acid at ordered mesoporous carbon functionalized with ferrocenecarboxylic acid-modified electrode. *Biosens. Bioelectron.* **2008**, *23*, 1680–1685.
23. Wu, L.; Feng, L.; Ren, J.; Qu, X. Electrochemical detection of dopamine using porphyrin-functionalized graphene. *Biosens. Bioelectron.* **2012**, *34*, 57–62.
24. Wu, S.; Wang, T.; Gao, Z.; Xu, H.; Zhou, B.; Wang, C. Selective detection of uric acid in the presence of ascorbic acid at physiological pH by using a β-cyclodextrin modified copolymer of sulfanilic acid and N-acetylaniline. *Biosens. Bioelectron.* **2008**, *23*, 1776–1780.
25. Xiao, C.; Chu, X.; Yang, Y.; Li, X.; Zhang, X.; Chen, J. Hollow nitrogen-doped carbon microspheres pyrolyzed from self-polymerized dopamine and its application in simultaneous electrochemical determination of uric acid, ascorbic acid and dopamine. *Biosens. Bioelectron.* **2011**, *26*, 2934–2939.

26. Özcan, A.; Şahin, Y. Preparation of selective and sensitive electrochemically treated pencil graphite electrodes for the determination of uric acid in urine and blood serum. *Biosens. Bioelectron.* **2010**, *25*, 2497–2502.
27. Wayu, M.B.; Schwarzmann, M.A.; Gillespie, S.D.; Leopold, M.C. Enzyme-free uric acid electrochemical sensors using β-cyclodextrin-modified carboxylic acid-functionalized carbon nanotubes. *J. Mater. Sci.* **2017**, *52*, 6050–6062.
28. Solangi, A.G.; Pirzada, T.; Shah, A.A.; Halepoto, I.A.; Chang, A.S.; Solangi, Z.A.; Solangi, M.Y.; Aftab, U.; Tonezzer, M.; Tahira, A. Phytochemicals of mustard (*Brassica Campestris*) leaves tuned the nickel-cobalt bimetallic oxide properties for enzyme-free sensing of glucose. *J. Chin. Chem. Soc.* **2022**, *69*, 1608–1618.
29. Ding, R.; Qi, L.; Jia, M.; Wang, H. Facile synthesis of mesoporous spinel $NiCo_2O_4$ nanostructures as highly efficient electrocatalysts for urea electro-oxidation. *Nanoscale* **2014**, *6*, 1369–1376.
30. Prathap, M.A.; Satpati, B.; Srivastava, R. Facile preparation of β-$Ni(OH)_2$-$NiCo_2O_4$ hybrid nanostructure and its application in the electro-catalytic oxidation of methanol. *Electrochim. Acta* **2014**, *130*, 368–380.
31. Qian, L.; Gu, L.; Yang, L.; Yuan, H.; Xiao, D. Direct growth of $NiCo_2O_4$ nanostructures on conductive substrates with enhanced electrocatalytic activity and stability for methanol oxidation. *Nanoscale* **2013**, *5*, 7388–7396.
32. Wu, X.; Han, Z.; Zheng, X.; Yao, S.; Yang, X.; Zhai, T. Core-shell structured Co_3O_4@$NiCo_2O_4$ electrodes grown on flexible carbon fibers with superior electrochemical properties. *Nano Energy* **2017**, *31*, 410–417.
33. Xu, K.; Yang, X.; Yang, J.; Hu, J. Synthesis of hierarchical Co_3O_4@$NiCo_2O_4$ core-shell nanosheets as electrode materials for supercapacitor application. *J. Alloys Compd.* **2017**, *700*, 247–251.
34. Zhang, G.; Wang, T.; Yu, X.; Zhang, H.; Duan, H.; Lu, B. Nanoforest of hierarchical Co_3O_4@$NiCo_2O_4$ nanowire arrays for high-performance supercapacitors. *Nano Energy* **2013**, *2*, 586–594.
35. Zhou, Y.; Ma, L.; Gan, M.; Ye, M.; Li, X.; Zhai, Y.; Yan, F.; Cao, F. Monodisperse MnO_2@$NiCo_2O_4$ core/shell nanospheres with highly opened structures as electrode materials for good-performance supercapacitors. *Appl. Surf. Sci.* **2018**, *444*, 1–9.
36. Jokar, E.; Zad, A.I.; Shahrokhian, S. Synthesis and characterization of $NiCo_2O_4$ nanorods for preparation of supercapacitor electrodes. *J. Solid State Electrochem.* **2015**, *19*, 269–274.
37. Chu, Q.; Yang, B.; Wang, W.; Tong, W.; Wang, X.; Liu, X.; Chen, J. Fabrication of a Stainless-Steel-Mesh-Supported Hierarchical Fe_2O_3@$NiCo_2O_4$ Core-Shell Tubular Array Anode for Lithium-Ion Battery. *ChemistrySelect* **2016**, *1*, 5569–5573.
38. Huang, G.; Zhang, L.; Zhang, F.; Wang, L. Metal–organic framework derived Fe_2O_3@$NiCo_2O_4$ porous nanocages as anode materials for Li-ion batteries. *Nanoscale* **2014**, *6*, 5509–5515.
39. He, Q.; Liu, J.; Liu, X.; Li, G.; Chen, D.; Deng, P.; Liang, J. Fabrication of amine-modified magnetite-electrochemically reduced graphene oxide nanocomposite modified glassy carbon electrode for sensitive dopamine determination. *Nanomaterials* **2018**, *8*, 194.
40. Gutiérrez, R.M.P.; Perez, R.L. Raphanus sativus (Radish): Their chemistry and biology. *Sci. World J.* **2004**, *4*, 811.
41. Hanlon, P.R.; Barnes, D.M. Phytochemical composition and biological activity of 8 varieties of radish (*Raphanus sativus* L.) sprouts and mature taproots. *J. Food Sci.* **2011**, *76*, C185–C192.
42. Nawaz, H.; Shad, M.A.; Rauf, A. Optimization of extraction yield and antioxidant properties of Brassica oleracea Convar Capitata Var L. leaf extracts. *Food Chem.* **2018**, *242*, 182–187.
43. Amin, S.; Tahira, A.; Solangi, A.R.; Mazzaro, R.; Ibupoto, Z.H.; Fatima, A.; Vomiero, A. Functional nickel oxide nanostructures for ethanol oxidation in alkaline media. *Electroanalysis* **2020**, *32*, 1052–1059.
44. Ibupoto, Z.H.; Tahira, A.; Shah, A.A.; Aftab, U.; Solangi, M.Y.; Leghari, J.A.; Samoon, A.H.; Bhatti, A.L.; Bhatti, M.A.; Mazzaro, R. $NiCo_2O_4$ nanostructures loaded onto pencil graphite rod: An advanced composite material for oxygen evolution reaction. *Int. J. Hydrog. Energy* **2022**, *47*, 6650–6665.
45. Li, W.; Zhang, B.; Lin, R.; Ho-Kimura, S.; He, G.; Zhou, X.; Hu, J.; Parkin, I.P. A dendritic nickel cobalt sulfide nanostructure for alkaline battery electrodes. *Adv. Funct. Mater.* **2018**, *28*, 1705937.
46. Wang, N.; Hang, T.; Chu, D.; Li, M. Three-dimensional hierarchical nanostructured Cu/Ni–Co coating electrode for hydrogen evolution reaction in alkaline media. *Nano-Micro Lett.* **2015**, *7*, 347–352.
47. López-Tinoco, J.; Mendoza-Cruz, R.; Bazán-Díaz, L.; Karuturi, S.C.; Martinelli, M.; Cronauer, D.C.; Kropf, A.J.; Marshall, C.L.; Jacobs, G. The preparation and characterization of Co–Ni nanoparticles and the testing of a heterogenized Co–Ni/alumina catalyst for CO hydrogenation. *Catalysts* **2019**, *10*, 18.
48. Lei, Y.; Li, J.; Wang, Y.; Gu, L.; Chang, Y.; Yuan, H.; Xiao, D. Rapid microwave-assisted green synthesis of 3D hierarchical flower-shaped $NiCo_2O_4$ microsphere for high-performance supercapacitor. *ACS Appl. Mater. Interfaces* **2014**, *6*, 1773–1780.
49. Marco, J.; Gancedo, J.; Gracia, M.; Gautier, J.; Ríos, E.; Berry, F. Characterization of the nickel cobaltite, NiCo2O4, prepared by several methods: An XRD, XANES, EXAFS, and XPS study. *J. Solid State Chem.* **2000**, *153*, 74–81.
50. Lv, J.; Li, C.; Feng, S.; Chen, S.-M.; Ding, Y.; Chen, C.; Hao, Q.; Yang, T.-H.; Lei, W. A novel electrochemical sensor for uric acid detection based on PCN/MWCNT. *Ionics* **2019**, *25*, 4437–4445.
51. Tsierkezos, N.G.; Ritter, U.; Thaha, Y.N.; Downing, C.; Szroeder, P.; Scharff, P. Multi-walled carbon nanotubes doped with boron as an electrode material for electrochemical studies on dopamine, uric acid, and ascorbic acid. *Microchim. Acta* **2016**, *183*, 35–47.

52. Wang, C.; Du, J.; Wang, H.; Zou, C.e.; Jiang, F.; Yang, P.; Du, Y. A facile electrochemical sensor based on reduced graphene oxide and Au nanoplates modified glassy carbon electrode for simultaneous detection of ascorbic acid, dopamine and uric acid. *Sens. Actuators B Chem.* **2014**, *204*, 302–309.
53. Ma, L.; Zhang, Q.; Wu, C.; Zhang, Y.; Zeng, L. PtNi bimetallic nanoparticles loaded MoS2 nanosheets: Preparation and electrochemical sensing application for the detection of dopamine and uric acid. *Anal. Chim. Acta* **2019**, *1055*, 17–25.
54. Hassanvand, Z.; Jalali, F. Simultaneous determination of l-DOPA, l-tyrosine and uric acid by cysteic acid-modified glassy carbon electrode. *Mater. Sci. Eng. C* **2019**, *98*, 496–502.
55. Li, L.; Wang, Y.; Pan, L.; Shi, Y.; Cheng, W.; Shi, Y.; Yu, G. A nanostructured conductive hydrogels-based biosensor platform for human metabolite detection. *Nano Lett.* **2015**, *15*, 1146–1151.
56. Guan, H.; Peng, B.; Gong, D.; Han, B.; Zhang, N. Electrochemical Enhanced Detection of Uric Acid Based on Peroxidase-like Activity of Fe_3O_4@Au. *Electroanalysis* **2021**, *33*, 1736–1745.
57. Wu, Y.Q.; Chen, X.Y.; Ji, P.T.; Zhou, Q.Q. Sol–gel approach for controllable synthesis and electrochemical properties of $NiCo_2O_4$ crystals as electrode materials for application in supercapacitors. *Electrochim. Acta* **2011**, *56*, 7517–7522.
58. Chang, A.S.; Tahira, A.; Chang, F.; Memon, N.N.; Nafady, A.; Kasry, A.; Ibupoto, Z.H. Silky Co_3O_4 nanostructures for the selective and sensitive enzyme free sensing of uric acid. *RSC Adv.* **2021**, *11*, 5156–5162.
59. Erden, P.E.; Kaçar, C.; Öztürk, F.; Kılıç, E. Amperometric uric acid biosensor based on poly (vinylferrocene)-gelatin-carboxylated multiwalled carbon nanotube modified glassy carbon electrode. *Talanta* **2015**, *134*, 488–495.
60. Li, H.; Wang, Y.; Ye, D.; Luo, J.; Su, B.; Zhang, S.; Kong, J. An electrochemical sensor for simultaneous determination of ascorbic acid, dopamine, uric acid and tryptophan based on MWNTs bridged mesocellular graphene foam nanocomposite. *Talanta* **2014**, *127*, 255–261.
61. Mobili, R.; Preda, G.; La Cognata, S.; Toma, L.; Pasini, D.; Amendola, V. Chiroptical sensing of perrhenate in aqueous media by a chiral organic cage. *Chem. Commun.* **2022**, *58*, 3897–3900.